

Efficient Electrocatalytic Nitrate Reduction to Ammonia Based on DNA-Templated Copper Nanoclusters

Wenjie Luo, Shilu Wu, Yingyang Jiang, Peng Xu, Jinxuan Zou, Jinjie Qian, Xuemei Zhou, Yongjie Ge,* Huagui Nie,* and Zhi Yang*



Cite This: *ACS Appl. Mater. Interfaces* 2023, 15, 18928–18939



Read Online

ACCESS |



Metrics & More



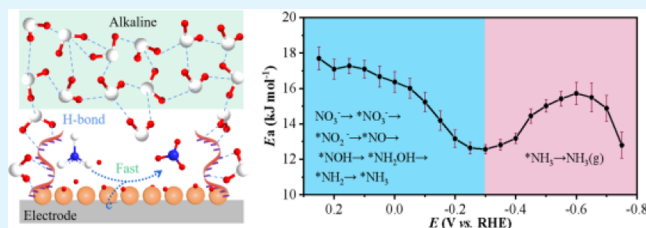
Article Recommendations



Supporting Information

ABSTRACT: In alkaline solutions, the electrocatalytic conversion of nitrates to ammonia (NH_3) (NO_3RR) is hindered by the sluggish hydrogenation step due to the lack of protons on the electrode surface, making it a grand challenge to synthesize NH_3 at a high rate and selectivity. Herein, single-stranded deoxyribonucleic acid (ssDNA)-templated copper nanoclusters (CuNCs) were synthesized for the electrocatalytic production of NH_3 . Because ssDNA was involved in the optimization of the interfacial water distribution and H-bond network connectivity, the water-electrolysis-induced proton generation was enhanced on the electrode surface, which facilitated the NO_3RR kinetics. The activation energy (E_a) and in situ spectroscopy studies adequately demonstrated that the NO_3RR was exothermic until NH_3 desorption, indicating that, in alkaline media, the NO_3RR catalyzed by ssDNA-templated CuNCs followed the same reaction path as the NO_3RR in acidic media. Electrocatalytic tests further verified the efficiency of ssDNA-templated CuNCs, which achieved a high NH_3 yield rate of $2.62 \text{ mg h}^{-1} \text{ cm}^{-2}$ and a Faraday efficiency of 96.8% at -0.6 V vs reversible hydrogen electrode. The results of this study lay the foundation for engineering catalyst surface ligands for the electrocatalytic NO_3RR .

KEYWORDS: nitrate reduction, electrocatalysis, ammonia, single-stranded DNA, copper nanocluster



1. INTRODUCTION

Ammonia (NH_3) plays important roles as an indispensable chemical raw material and an ideal hydrogen-storage carrier in industrial production and practical applications.^{1–3} Currently, industrial NH_3 synthesis mainly relies on the energy- and carbon-emission-intensive Haber–Bosch (H–B) process.⁴ An alternative route is to utilize sustainable electrical power to convert waste nitrates into value-added NH_3 through a nitrate reduction reaction (NO_3RR) under ambient conditions and restore the imbalance in the global nitrogen cycle.^{5–7} The NO_3RR is a multielectron-coupled proton-transfer process, which inevitably generates some undesirable byproducts, such as nitrogen oxyanions and dinitrogen.^{8–10} Therefore, the rational design and development of efficient catalysts to improve the efficiency and selectivity of nitrate-to- NH_3 conversion is highly desirable.

Cu-based catalysts are abundant, readily available, and inexpensive. These advantages and the similar energy levels of the Cu d and nitrate π^* lowest unoccupied molecular orbitals make Cu-based catalysts very promising to promote the NO_3RR thermodynamics and kinetics under ambient conditions.^{11–13} Recently, theoretical and experimental studies have found that, in acidic solutions, the Cu-catalyzed NO_3RR is exothermic until NH_3 desorption.^{14–16} In contrast, due to the lack of protons, the NO_3RR thermodynamics and kinetics are limited by the sluggish hydrogenation of $^*\text{NO} \rightarrow ^*\text{NOH}$ in

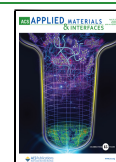
alkaline solutions. When the hydrogenation step of $^*\text{NO}$ is hindered, $^*\text{NO}$ will be reduced to dissociated $^*\text{N}$ or react with NO dissolved in solution to produce $^*\text{N}_2\text{O}$, which is conducive to nitrogen generation.^{17,18} It follows that the slow hydrogenation $^*\text{NO} \rightarrow ^*\text{NOH}$ in alkaline solutions reduces the NH_3 selectivity of the catalyst. However, because the NO_3RR is restrained by excessive hydrogen evolution reaction (HER) under acidic conditions, the former is usually performed in alkaline solutions. A substantial effort has been made to improve the poor hydrogenation capabilities of Cu-based catalysts in alkaline solutions by alloying Cu with noble/transition metals (e.g., Ni, Pd, and Ru)^{19–23} or forming hybrids with metal oxides (e.g., Cu_2O).²⁴ Although these strategies exhibit efficient electrocatalytic performances for NH_3 production, their catalytic activities remain limited by proton generation on the electrode surface.

Numerous recent studies have revealed that, in alkaline solutions, protons originate from dissociation of the water molecules closest to the electrode surface.^{25–28} However,

Received: January 12, 2023

Accepted: March 23, 2023

Published: April 4, 2023



discontinuous H-bond networks near the electrode surface decrease the water concentration and limit proton generation.²⁵ Therefore, the kinetics of proton-coupled electron-transfer reactions are severely limited. In contrast, the kinetics are improved by constructing continuous H-bond networks on the catalyst surface. In biological systems, efficient proton/water transfer can be achieved by forming peptide chains around the active sites of metalloproteins (such as hydrogenases and cytochrome *c* oxidases).^{29–32} One end of these flexible peptide chains is attached to the active site, while the other end can be extended to transport distant protons/water molecules to the active site through continuous H-bond chains formed by polar amino acids bound with hydronium ions or water molecules.^{33,34} Inspired by the proton/water transfer in biological systems, we speculate that using macromolecules containing numerous polar groups to assist Cu-based catalysts would improve the poor hydrogenation capabilities of bare Cu in alkaline solutions. As a biomacromolecule, deoxyribonucleic acid (DNA) is a potential molecule for building continuous H-bond chains because of its abundance of polar functional groups, long chains, and immobilization and functionalization capabilities. Additionally, it has been demonstrated that single-stranded DNA polythymine (ssDNA poly-T) can be used as a template for synthesizing copper nanoclusters (CuNCs) with ultrasmall size (<2 nm), abundant active sites, and molecular-like discrete energy levels.^{35,36} Thus, ssDNA poly-T-templated CuNCs may exhibit efficient electrocatalytic activity for the NO₃RR under ambient conditions. Nevertheless, to the best of our knowledge, the CuNC-induced electrocatalytic conversion of nitrates to NH₃ has seldom been reported.³⁷

Therefore, we synthesized CuNCs using 40-thymine-containing ssDNA as templates (labeled as “T40-CuNCs”) to enhance the NO₃RR. The T40 chain sections that were unbound to CuNCs could extend into the bulk electrolyte and construct a continuous H-bond network. The T40-CuNCs polar groups could capture water molecules and directionally transport them to the catalyst surface to facilitate proton generation on the electrode surface. Consequently, the NO₃RR hydrogenation step was accelerated drastically. Therefore, the as-designed T40-CuNCs electrocatalyst enhanced the full-range NO₃RR kinetics compared to those of the bare Cu catalyst (Figure 1), thereby converting nitrates to NH₃ with a high Faraday efficiency (FE) of 96.8% and a NH₃ yield rate of 2.62 mg h⁻¹ cm⁻² at -0.6 V vs reversible hydrogen electrode (RHE).

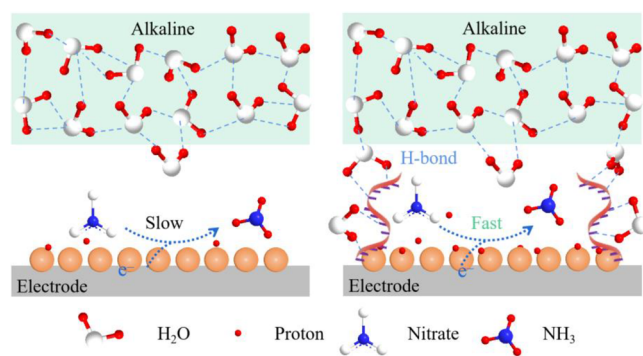


Figure 1. Schematics of the conversion of nitrate to NH₃ electrocatalyzed by (left) conventional Cu and (right) T40-CuNCs in alkaline solution.

2. RESULTS AND DISCUSSION

We synthesized T40-CuNCs as an electrocatalyst for enhancing the NO₃RR. The T40-CuNCs synthesis is schematically illustrated in Figure 2a. Briefly, T40-complexed Cu²⁺ (labeled as “T40-Cu²⁺”) was reduced using ascorbate to form the T40-CuNCs. The average T40-CuNCs particle size was ~1.9 nm, as determined via transmission electron microscopy (TEM; Figures 2b and S1). The high-resolution TEM (HRTEM) image of T40-CuNCs exhibits a lattice fringe distance of 0.21 nm, which corresponds to the Cu(111) plane. However, the acquired X-ray diffraction (XRD) patterns (Figure S2) did not exhibit any identifiable peaks because the T40-CuNCs were very small, which is consistent with previous reports.³⁸ Furthermore, T40-CuNCs exhibited strong fluorescence emission with excitation and emission bands at 370 and 630 nm, respectively (Figure 2c), which is consistent with the fluorescence emission of metal NCs of <2 nm³⁶ and indicates that ultrasmall T40-CuNCs were synthesized.

To determine which T40 sites were bound with Cu, we conducted Raman spectroscopy, Fourier transform infrared (FTIR), and X-ray photoelectron spectroscopy (XPS) studies. As shown in Figure 2d, compared to the Raman spectrum of T40, that of the T40-Cu²⁺ complexes exhibits a band at ~501 cm⁻¹, which is attributed to Cu²⁺-O.^{39,40} Additionally, the band at ~614 cm⁻¹, attributed to the thymine N-C-O, shifted to lower wavenumbers.⁴¹ After ascorbate was added, the Cu²⁺-O band at ~501 cm⁻¹ disappeared, and the Cu-O band^{42,43} appeared at ~622 cm⁻¹, indicating that ascorbate reduced the Cu²⁺ ions to atomic Cu. Additionally, the FTIR and XPS spectra revealed that the thymine carbonyl vibration peak at 1640 cm⁻¹ shifted (Figure 2e), and the O 2p binding energy of C=O-NH in the T40-CuNCs drastically decreased (Figure S3). These results indicate that the thymine carbonyl O atom is bound to Cu, which is consistent with previous reports.³⁶ Additionally, Figure S4 shows that the nucleotide absorption band (260 nm)⁴⁴ of T40-CuNCs changed negligibly compared to T40. Moreover, T40 and T40-CuNCs exhibited similar circular dichroism spectra, indicating that the T40 secondary structure did not change during the CuNCs formation.⁴⁵ These results suggest that the reductant neither damaged nor reshaped the T40 structure.

To investigate the NO₃RR activity of the T40-CuNCs under ambient conditions, electrocatalysis was performed in a customized H-cell fabricated using a traditional three-electrode system. Additionally, T20-CuNCs, T60-CuNCs (prepared using 20- or 60-thymine-containing ssDNA templates, respectively), and copper nanoparticles (CuNPs) with average sizes of 2.4, 3.1, and 6.8 nm were prepared for comparison (Figure S5). The T20-CuNCs and T60-CuNCs HRTEM images exhibit a 0.21 nm lattice fringe, which corresponds to the Cu(111) plane. The CuNPs HRTEM image exhibits 0.21 and 0.18 nm lattice fringes, which correspond to the Cu(111) and Cu(200) planes, respectively, and are consistent with the XRD patterns (Figure S6).

Figure 3a presents the linear-sweep voltammetry (LSV) curves of the as-synthesized catalysts in a 1 M KOH electrolyte prepared with or without KNO₃. In the KNO₃-containing electrolyte, all of the catalysts exhibited enhanced current densities compared to those of the catalysts in the nitrate-free electrolyte. As the potential became more negative, although HER occurred, the NO₃RR was predominant, as evidenced by comparing the NO₃RR and HER current densities at -0.6 V vs

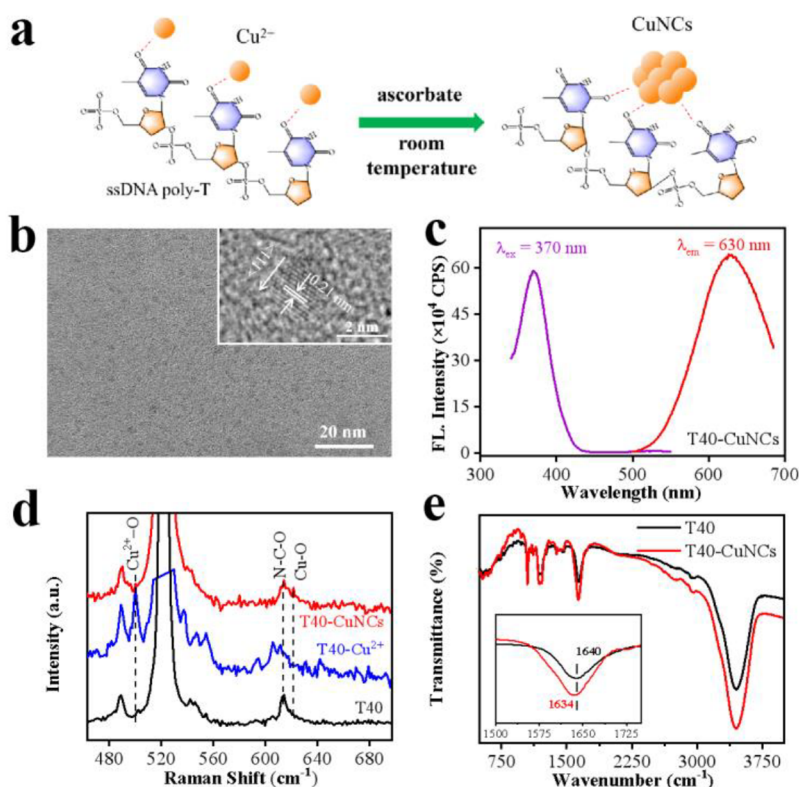


Figure 2. (a) Schematic showing the synthesis of T40-CuNCs by reducing T40-complexed Cu^{2+} ions. (b) TEM and (inset) HRTEM images of T40-CuNCs. (c) Fluorescence spectra of T40-CuNCs. (d) Raman spectra for T40, T40- Cu^{2+} , and T40-CuNCs. (e) FTIR spectra for T40 and T40-CuNCs.

RHE (Figure 3b). The ssDNA poly-T-decorated CuNCs (T-CuNCs) exhibited higher NO_3RR and HER current densities than the CuNPs at -0.6 V, indicating that the CuNCs catalytic activity outperformed the CuNPs catalytic activity for both the NO_3RR and HER partly because the CuNCs prepared using the ssDNA poly-T template were smaller and exhibited more active sites than the CuNPs. More importantly, the sections of ssDNA poly-T that were unbound to the CuNCs extended into the bulk electrolyte to construct a continuous H-bond network, which improved the interfacial water-molecule distribution and electrolysis and thus accelerated the HER and NO_3RR . This result was further confirmed by analyzing the Tafel slopes and electrochemically active surface areas (ECSAs). The CuNPs Tafel slopes were 572.2 and 372.5 mV dec^{-1} for the HER and NO_3RR , respectively, which were steeper than those of T20-CuNCs (509.4 and 266.0 mV dec^{-1}), T40-CuNCs (335.9 and 275.8 mV dec^{-1}), and T60-CuNCs (314.9 and 281.5 mV dec^{-1}) in the same overpotential interval, as shown in Figure 3c,d. Meanwhile, the CuNPs exhibited a smaller ECSA than those of the different CuNCs for the NO_3RR (Figures S7 and 3e). The HER current densities gradually increased with increasing ssDNA poly-T chain length because the longer ssDNA poly-T chain contained more polar groups and was more conducive to proton enrichment on the electrode surface. However, because the excessive HER restrained the NO_3RR , the NO_3RR current density of the T60-CuNCs decreased rather than increased compared with that of the T40-CuNCs at -0.6 V. Due to abundant active sites and an appropriately improved proton concentration on the catalyst surface, the T40-CuNCs may be ideal electrocatalysts for converting nitrates to NH_3 . As shown

in Figure S8, the T40 and T40-CuNCs exhibited similar catalytic activities for the HER. In contrast, the NO_3RR performance on the T40-CuNCs surface outperformed that on the T40 one. Apparently, at -0.6 V vs RHE, the FE and NH_3 yield rates of the T40-CuNCs were considerably higher than those of T40, indicating that the catalytic activity of the T40-CuNCs for the NO_3RR mainly originated from the CuNCs. The role of T40 is to enhance the connectivity of H-bond networks and facilitate proton generation.

The product selectivity was analyzed by holding a certain potential for 1 h further to determine the catalytic activity of the T40-CuNCs for the NO_3RR , and the generated NH_3 products were quantified using ultraviolet–visible (UV–vis) and ^1H NMR spectroscopies (Figure S9). The NH_4^+ concentrations determined by ^1H NMR and UV–vis spectroscopies were consistent. Parts f and g of Figure 3 show the catalyst FEs and NH_3 yield rates obtained at different potentials. Among all catalysts, the T40-CuNCs exhibited the highest FEs and NH_3 yield rates in the tested potential windows. The FEs of the T40-CuNCs continuously increased with negatively moving potential and reached a maximum of 96.8% at -0.6 V, and the corresponding NH_3 yield rates was 2.62 $\text{mg h}^{-1} \text{cm}^{-2}$. In the whole tested potential range, the T40-CuNCs exhibited a lower NO_2^- yield rate and FE compared to those of CuNPs, indicating that the T40-CuNCs efficiently catalyzed the conversion of NO_2^- to NH_3 (Figure S10). Figure S11 shows that the NH_4^+ selectivity of the T40-CuNCs highly depends on the applied potential. Apparently, a NH_4^+ selectivity above 91.1% was attained at -0.6 V vs RHE, indicating that $\sim 91.1\%$ of the nitrate was converted to NH_3 . In contrast, the NO_2^- and other N-containing species selectivities

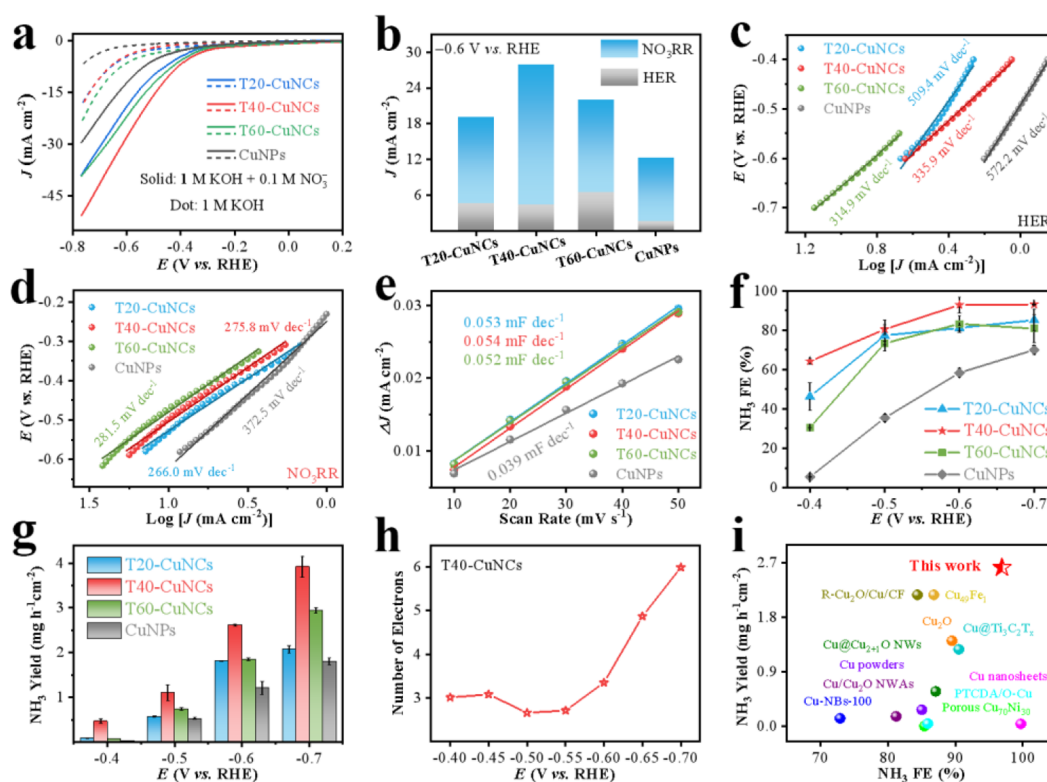


Figure 3. Electrocatalytic conversion of nitrates to NH_3 . (a) LSV curves of the as-synthesized catalysts in a 1 M KOH electrolyte prepared with and without KNO_3 . (b) Current densities for the NO_3RR and HER collected at -0.6 V. (c and d) Tafel slopes for the HER and NO_3RR extracted from the LSV curves. (e) ECSAs, (f) FEs, and (g) NH_3 yield rates of the as-synthesized catalysts in a solution comprising 1 M KOH and 0.1 M NO_3^- . (h) Number of electrons associated with the NO_3RR at each potential. (i) Comparison of the FEs and NH_3 yield rates for the NO_3RR catalyzed by different Cu-based catalysts.

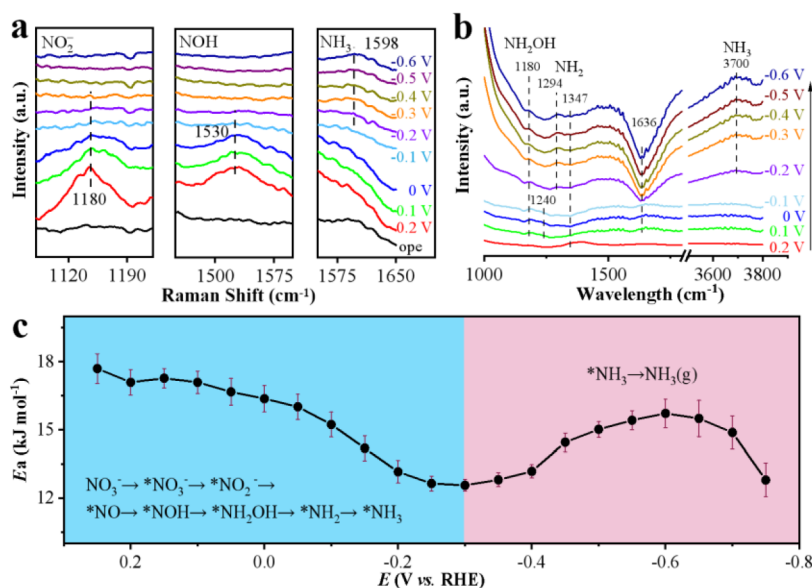


Figure 4. Mechanism for the NO_3RR catalyzed by the T40-CuNCs. Electrochemical in situ (a) Raman and (b) FTIR spectra of the T40-CuNCs at different potentials in a solution comprising 1 M KOH and 0.1 M NO_3^- . (c) T40-CuNCs catalyzed activation energy for the NO_3RR at various potentials.

were as low as 8.87%. Figure S12 shows that the pH changed negligibly during nitrate reduction at -0.6 V vs RHE in a solution comprising 1 M KOH and 0.1 M KNO_3 .

Due to the high catalytic activity of the CuNCs, a satisfactory catalytic performance can be obtained using only

a tiny mass of the catalyst. Therefore, the T40-CuNCs mass activity for yielding NH_3 was as high as $2.71 \text{ g h}^{-1} \text{ mg}_{\text{Cu}}^{-1}$ (Figure S13). As expected, the T40-CuNCs were also highly efficient for the NO_3RR in neutral media, revealing a maximum NH_3 yield rate of $1.12 \text{ mg h}^{-1} \text{ cm}^{-2}$ and a high FE of 95.3% at

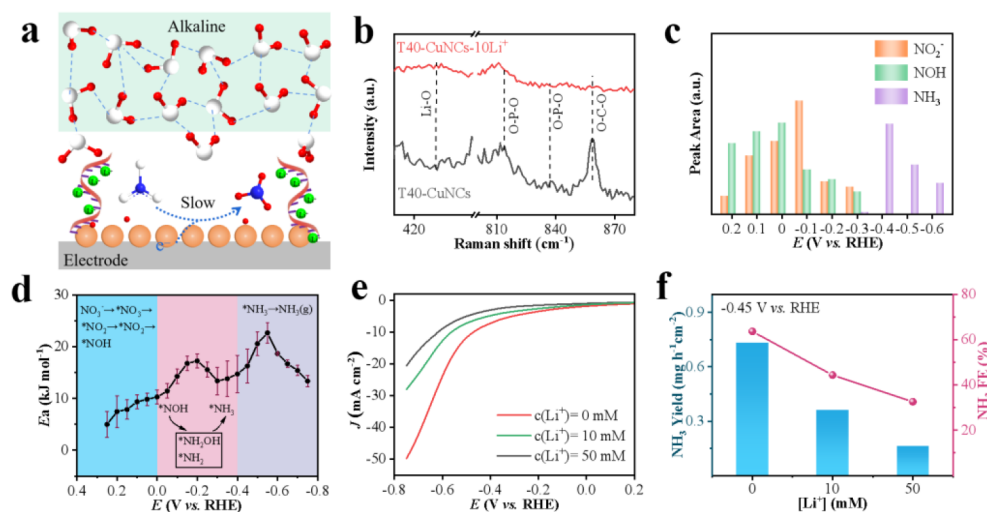


Figure 5. Proof of the proton-transfer function of T40. (a) Schematics of the Li^+ ion shielding experiment. (b) Raman spectra of the T40-CuNCs and T40-CuNCs-10 Li^+ . (c) Change tendency of the relative Raman signal for NO_2^- , NOH, and NH_3 as a function of the applied potential extracted from the in situ Raman spectra shown in Figure S21. (d) T40-CuNCs-10 Li^+ -catalyzed activation energy for the NO_3RR at various potentials. (e) LSV curves and (f) FEs and NH_3 yield rates of the T40-CuNCs with and without Li^+ shielding in a 1 M KOH + 0.1 M NO_3^- solution.

−0.6 V (Figure S14). However, in acidic media, the NH_3 yield rate (0.63 $\text{mg h}^{-1} \text{cm}^{-2}$) and FE (28.4%) were far from satisfactory due to the increased competitiveness of the HER. In addition, controlled experiments were conducted to confirm that NH_3 was produced from NO_3^- reduction on the T40-CuNCs surface. As shown in Figure S15a, the negligible NH_3 yield rate of the T40-CuNCs (<0.026 $\text{mg h}^{-1} \text{cm}^{-2}$) was measured without NO_3^- . Moreover, an isotope tracing experiment was performed using $^{15}\text{NO}_3^-$ as the reactant. As shown in Figure S15b, the isotope tracing of $^{15}\text{NH}_3$ produced using $^{15}\text{NO}_3^-$ exhibited two peaks, while that of $^{14}\text{NH}_3$ produced using $^{14}\text{NO}_3^-$ exhibited three peaks, indicating that NH_3 was indeed generated from nitrate rather than other impurities.⁴⁶

To elucidate the number of NO_3RR -associated electrons, we measured the rotating-disk electrode (RDE) voltammograms of the T40-CuNCs in a solution comprising 10 mM KNO_3 and 1 M KOH (Figure S16a). Additionally, the Koutecký–Levich (K–L) curves obtained at different potentials are shown in Figure S16b. The K–L analysis revealed that the number of electrons (n) in the reaction increased with the increasingly negative test potential and that $n = 4.7$ at −0.65 V, suggesting that the electrocatalytic conversion of nitrates to NH_3 was enhanced (Figure 3h). The experimental n value deviating from the theoretical one may be due to the different mechanistic pathways.⁴⁷ Impressively, the FEs and NH_3 yield rates of the T40-CuNCs compared favorably with those of other previously reported Cu-based catalysts (Figure 3i).^{24,48–57}

We performed in situ Raman measurements to provide further insight into the NO_3RR mechanism. Figures S18 and 4a present the Raman spectra obtained during nitrate reduction on the T40-CuNCs surface from +0.2 to −0.6 V (bottom and top, respectively). The peaks observed at 1180, 1370, 1530, and 1598 cm^{-1} are associated with the symmetric N–O stretches of adsorbed NO_2^- , antisymmetric N–O stretches of adsorbed nitrate, N=O stretches of NOH, and H–N–H deformation of NH_3 , respectively.^{58,59} Additionally, a weak shoulder peak observed at ~1530 cm^{-1} is attributed to a

combined NOH stretching and bending mode. Figure S19 shows the Raman peak areas for NO_2^- , NOH, and NH_3 plotted as functions of the applied potential. Evidently, only the NO_2^- and NOH Raman signals appeared in the applied potential range 0.2–0 V, and the intensity of the NO_2^- Raman signal weakened with the increasingly negative applied potential, indicating that NO_2^- was rapidly converted to NOH. As the applied potential became increasingly negative, the intensity of the NOH Raman signal rapidly weakened and an apparent NH_3 Raman signal appeared at −0.3 V, indicating that NOH was converted into adsorbed NH_3 in the applied potential range from 0 to −0.3 V.

The in situ FTIR spectra were generated for the T40-CuNCs to further probe the catalyst surfaces during the reaction. As shown in Figure 4b, the FTIR spectra of the T40-CuNCs exhibited bands at 1180, 1240, 1294, 1347, 1636, and 3700 cm^{-1} . At 0.2 V, an upward band attributed to NO_3^- appeared at 1347 cm^{-1} , indicating that NO_3^- began to adsorb on the catalyst surface. At 0.1 V, this absorption band changed to a negative band, indicating the consumption of NO_3^- in the solution.⁶⁰ Meanwhile, upward bands associated with the formation of NO_2^- and NH_2OH appeared at 1240 and 1180 cm^{-1} , respectively,^{58,61} which are crucial intermediates for NH_3 formation. As the potential moved toward −0.2 V vs RHE, a band corresponding to another key intermediate appeared at ~1294 cm^{-1} and was ascribed to NH_2 .⁶² Additionally, an upward band associated with NH_3 formation appeared at 3700 cm^{-1} , and the NO_2^- -related band at 1240 cm^{-1} disappeared.⁶³ The in situ FTIR spectroscopy analysis suggests that, at −0.2 V vs RHE, NO_2^- was rapidly converted to NH_3 through intermediates, such as NH_2OH and NH_2 . Additionally, the upward band at ~1636 cm^{-1} was attributed to water electrolysis, generating a proton during the NO_3RR .⁶⁴ The in situ FTIR spectra are consistent with the in situ Raman ones, indicating that the T40-CuNCs can accelerate the hydrogenation step of the NO_3RR . This is primarily due to the role of T40 in constructing a continuous H-bond network near the electrode surface, which facilitates water electrolysis to generate protons. From the combined electrochemical in situ

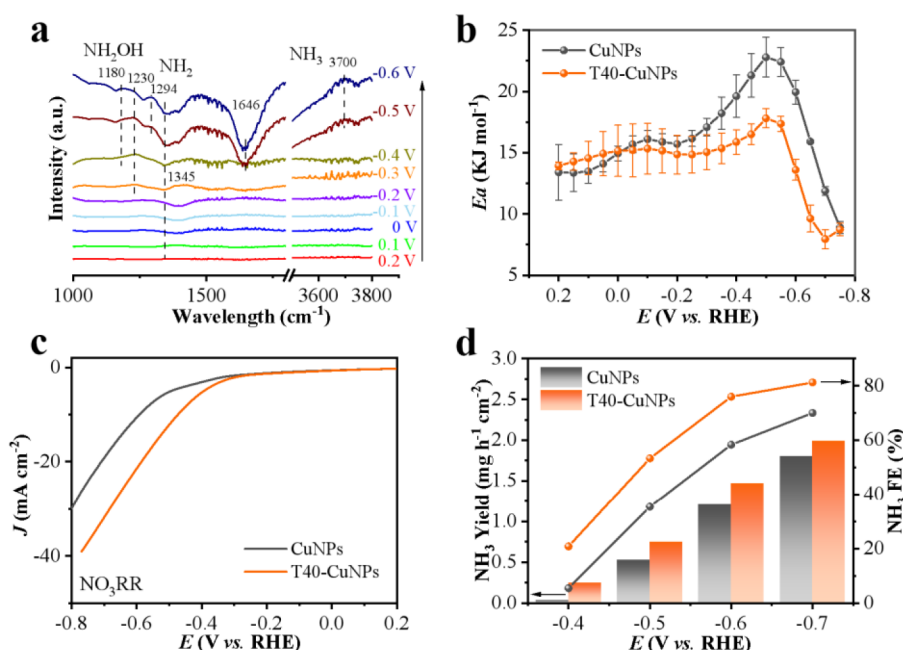


Figure 6. Role of T40 in the catalytic NO₃RR. (a) Electrochemical in situ FTIR spectra of CuNPs at different potentials in a solution comprising 1 M KOH and 0.1 M NO₃⁻. (b) CuNPs- and T40-CuNPs-catalyzed activation energy for the NO₃RR at various potentials. (c) LSV curves of the NO₃RR on CuNPs and T40-CuNPs. (d) NH₃ yield rates and FEs of CuNPs and T40-CuNPs.

FTIR and Raman spectroscopy analyses, the NO₃RR pathway on the T40-CuNCs surface was proposed as a series of deoxygenation reactions of NO₃⁻ → *NO₃⁻ → *NO₂⁻ → *NO, accompanied by a series of hydrogenation reactions of *NO → *NOH → *NH₂OH → *NH₂ → *NH₃.

Furthermore, we experimentally determined the activation energies (*E_a*) for the NO₃RR by analyzing the temperature-dependent kinetics of the T40-CuNCs catalyst.^{65–68} The LSV curves of the T40-CuNCs were recorded in a solution comprising 100 mM KNO₃ and 1 M KOH in the range 20–50 °C (Figure S20a). By fitting the current densities measured at different temperatures using the Arrhenius equation (Figure S20b), *E_a* values were obtained at each applied potential (Figure 4c). *E_a* decreased continuously when the applied potential went from positive to -0.3 V and then increased in the applied potential range from -0.3 to -0.6 V. The in situ FTIR and Raman spectra indicated that NO₃⁻ was converted to NH₃ at -0.3 V. Thus, the energy barrier of 15.72 kJ mol⁻¹ at -0.6 V vs RHE was not attributed to *NO₃⁻ → *NH₃. A previous study found that NH₃ desorption from the Cu electrode was an endothermic process.⁶⁰ Therefore, we deduced that the energy barrier at -0.6 V vs RHE was attributed to NH₃ desorption. Additionally, the *E_a* values indicated that overall the NO₃RR is exothermic before NH₃ desorption, which contradicts the NO₃RR in alkaline solutions but is consistent with it in acidic solutions. In alkaline environments, the RDS of the NO₃RR on bare Cu-based catalyst surfaces is *NO hydrogenation (i.e., *NO + H⁺ + e⁻ → *NOH) due to the lack of protons. In contrast, the continuous H-bond network ensures smooth progression of the NO₃RR in acidic media. Taken together, the in situ Raman and activation-energy studies sufficiently prove that the T40 chain can optimize the interfacial water-molecule distribution and H-bond network connectivity, which solves the NO₃RR problem in alkaline solutions and promotes NH₃ formation.

The continuous H-bond network constructed by T40 is based on the H bonds formed between the polar groups of T40 and water molecules. We performed the Li⁺ ions shielding experiments to verify the role of T40 in constructing the H-bond network and improving the electrocatalytic NO₃RR progress (Figure 5a). Briefly, Li⁺ is introduced to the electrolyte solution to shield the polar groups of T40 to prevent them from combining with water molecules. Figure 5b shows the Raman spectra of the T40-CuNCs and T40-CuNCs shielded by 10 mM Li⁺ (labeled as T40-CuNCs-10Li⁺). The characteristic Raman peaks of Li–O appear at 432 cm⁻¹,⁶⁹ and the peaks at 815/835 and 861 cm⁻¹ are assigned to the O–P–O backbone stretching and C–O–C stretching of T40 shifted and attenuated in the T40-CuNCs-10Li⁺ Raman spectrum.⁷⁰ This result indicates that Li⁺ occupies the polar groups of T40 and achieves the shielding effect. Subsequently, the in situ Raman spectra were obtained during nitrate reduction on the T40-CuNCs in a 1 M KOH electrolyte containing 100 mM NO₃⁻ and 10 mM Li⁺ under different applied potentials (Figure S21). Furthermore, variation of the NO₂⁻, NOH, and NH₃ Raman areas as applied potentials were extracted from the in situ Raman spectra (Figure 5c). The Raman signal of NO₂⁻ is continuously enhanced when the applied potential is positive to -0.1 V, indicating that the formation rate of NO₂⁻ is greater than the consumption rate, and its conversion to NOH is slow. The Raman signal of NOH decreased in the applied potential range of 0 to -0.3 V, but the NH₃ Raman signal was not detected, which indicates that NOH was converted to another intermediate product (such as NHOH, NH, and NH₂). When the potential is further swept to a more negative regime (<-0.4 V), a pronounced NH₃ Raman peak begins to appear, indicating that the primary reaction at this stage is the formation of NH₃. We also measured the *E_a* value of T40-CuNCs-10Li⁺ toward the NO₃RR at a different applied potentials (Figures S22). According to the results of the in situ Raman measurements, we ascribed the *E_a* value corresponding

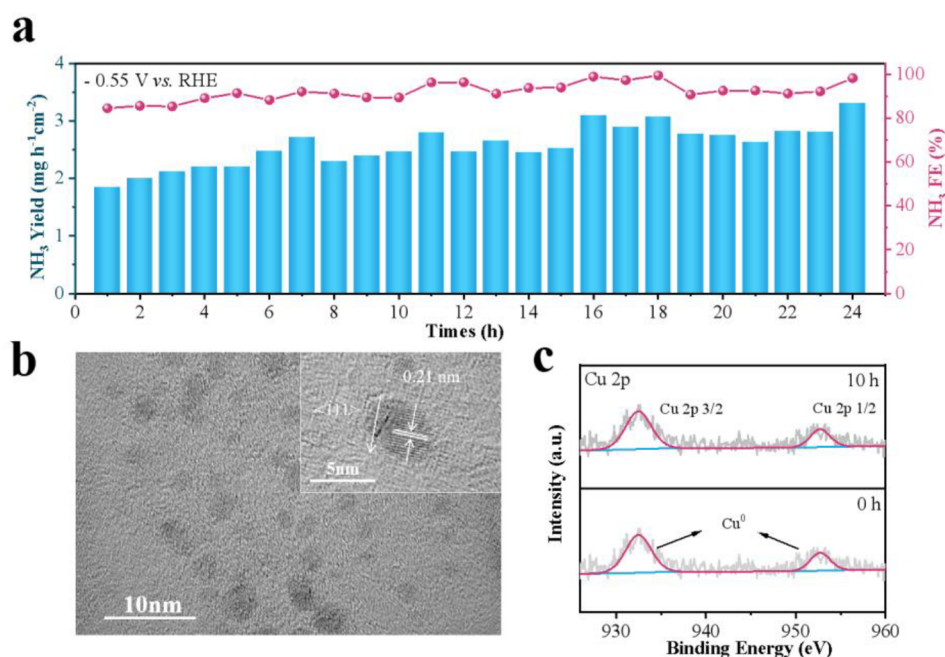


Figure 7. Catalytic stability of T40-CuNCs. (a) Cycling of the T40-CuNCs catalysts for 1 h at -0.55 V vs RHE for the NO_3RR in an electrolyte containing 1 M KOH and 0.1 M KNO_3 . (b) TEM image of the T40-CuNCs catalyst for the NO_3RR after 10 cycles. The inset presents an enlarged HRTEM image of the catalyst. (c) Cu 2p XPS spectra of the T40-CuNCs catalysts for the NO_3RR before and after 10 cycles.

to the reaction path. As shown in Figure 5d, the E_a value of NO_2^- conversions to NOH and the hydrogenation of NOH showed an upward trend, which is consistent with the NO_3RR process in an alkaline solution reported in the literature.¹⁵ These observations demonstrate that the polar group of T40 loses its construct H-bond network capability after combining with Li^+ ions, retarding the generation of protons on the electrode surface, resulting in the kinetics of the whole NO_3RR process, especially the hydrogenation step, slowing down.

We further examine the activity of the T40-CuNCs and T40-CuNCs- Li^+ toward the HER and NO_3RR . Obviously, the T40-CuNCs exhibited a reduced HER current and a greater Tafel slope after being shielded by Li^+ (Figure S23). Similarly, the LSV curves of the NO_3RR show that the current density decreases and the onset potential shifts toward a more negative direction with increasing Li^+ shield effect (Figure 5e). Moreover, the Tafel slope extracted from the LSV curves shows that the T40-CuNCs exhibited a minor Tafel slope of 275.9 mV dec^{-1} compared with 380.1 and 414.5 mV dec^{-1} for the T40-CuNCs shielded by 10 and 50 mM Li^+ , respectively (Figure S24). The NH_3 yield rates and FEs of the T40-CuNCs and T40-CuNCs shielded by 10 and 50 mM Li^+ are 0.73 $\text{mg h}^{-1} \text{cm}^{-2}/63.6\%$, 0.36 $\text{mg h}^{-1} \text{cm}^{-2}/44.3\%$, and 0.17 $\text{mg h}^{-1} \text{cm}^{-2}/32.6\%$ at -0.45 V, respectively. Apparently, introducing Li^+ ions slowed down the kinetics of the HER and NO_3RR reaction.

Apart from Li^+ ion shielding experiments, we analyzed the NO_3RR on CuNPs surfaces to fully demonstrate the role of T40 in promoting the NO_3RR . The in situ FTIR spectra of the CuNPs in Figure 6a show that the negative band at 1345 cm^{-1} was associated with NO_3^- consumption at 0 V vs RHE. However, the NO_2^- -formation-related upward band at 1230 cm^{-1} was detected until -0.3 V vs RHE, and no bands related to other N-containing species appeared, indicating that the reaction at >-0.3 V vs RHE was mainly $^*\text{NO}_3^- \rightarrow ^*\text{NO}_2^-$. The E_a study suggests that the energy barrier for $^*\text{NO}_3^- \rightarrow$

$^*\text{NO}_2^-$ is 16.11 kJ mol^{-1} (Figures S25 and 6b). As the potential moved negatively toward -0.5 V vs RHE, a very distinct water-electrolysis-associated band appeared at 1646 cm^{-1} , accompanied by bands at 1180 , 1294 , and 3700 cm^{-1} , which were attributed to the formation of NH_2OH , NH_2 , and NH_3 , respectively. These results show that water electrolysis on the electrode surface was highly correlated with the NO_3RR hydrogenation step. Notably, NH_3 formation and water electrolysis on the CuNPs surface was 300 mV more negative than that on the T40-CuNCs one, indicating that the latter exhibited superior kinetics. Meanwhile, the E_a study suggests that the energy barrier required for forming NH_3 on CuNPs was 22.79 kJ mol^{-1} , which is much higher than that required for forming NH_3 on T40-CuNCs (17.7 kJ mol^{-1}).

To further prove that T40 can promote water electrolysis and the NO_3RR , we self-assembled T40-CuNPs. Briefly, CuNPs-loaded carbon paper was immersed in the T40 solution for 1 h, rinsed with water, and dried in air to obtain T40-CuNPs. Obviously, the T40-CuNPs exhibited a higher HER current and a gentler Tafel slope than the pristine CuNPs (Figure S26). Additionally, at -0.5 V vs RHE, the E_a value of the T40-CuNPs catalyzing NH_3 formation decreased from 22.79 to 17.80 kJ mol^{-1} compared to that of pristine CuNPs (Figure 6b), and the NO_3RR current density increased (Figure 6c). Moreover, at -0.6 V vs RHE, the FEs and NH_3 yield rates of the T40-CuNCs were considerably superior to those of the CuNPs (Figure 6d). These results fully demonstrate that T40 can effectively enhance the NO_3RR because it promotes water electrolysis, resulting in a proton-rich electrode surface.⁷¹

In addition to the catalytic performance, the long-term stability of the catalysts is critical for practical applications. Figure 7a shows the cycling stability of the T40-CuNCs at an applied potential of -0.55 V for 1 h per cycle. Notably, the FEs and NH_3 yield rates remained stable without attenuation during the 24 cycles. Moreover, the HRTEM image shows that the cycled T40-CuNCs maintained the same morphology,

average size, and lattice fringes as the pristine ones (Figure 7b). The high-resolution Cu 2p XPS spectrum of the T40-CuNCs is segmented into two prominent peaks at 932.4 and 952.7 eV, which correspond to Cu⁰ 2p_{3/2} and Cu⁰ 2p_{1/2}, respectively. After the cycling tests, the XPS signal changed negligibly, indicating that Cu can maintain a stable valence state during cycling (Figure 7c). These results suggest that the T40-CuNCs exhibited excellent stability for electrocatalytically reducing nitrates to NH₃. The excellent stability of the T40-CuNCs for the electrocatalytic NO₃RR confirms that Cu negligibly forms soluble complexes with NH₃ because the formation of soluble complexes consumes the catalyst on the working electrode surface, which will drastically attenuate the T40-CuNCs catalytic activity for the NO₃RR.

3. CONCLUSIONS

Inspired by H-bond chains in biological systems, we synthesized T40-CuNCs as electrocatalysts for enhancing the NO₃RR. Because ssDNA optimized the interfacial water-molecule distribution and H-bond network connectivity, water-electrolysis-induced proton generation was enhanced on the electrode surface, which facilitated the NO₃RR kinetics. Consequently, the T40-CuNCs achieved a high NH₃ yield rate of 2.62 mg h⁻¹ cm⁻² and a FE of 96.8% at -0.6 V, thereby exhibiting intrinsically high reactivity for the NO₃RR. The results of this study provide insights for designing and optimizing catalysts for renewable energy applications.

4. EXPERIMENTAL SECTION

Materials. Oligonucleotides were purchased from Shanghai Sangon Biological Engineering Technology and Services Co., Ltd. (Shanghai, China). Potassium hydroxide (KOH), potassium nitrate (KNO₃), lithium nitrate (LiNO₃), sodium chloride (NaCl), copper sulfate (CuSO₄), 3-(*N*-morpholino)propanesulfonic acid (MOPS; C₇H₁₃NO₄S), and sodium ascorbate (C₆H₇NaO₆) were obtained from Sigma-Aldrich. All other reagents and chemicals were of analytical grade and were used as received without further purification. All aqueous solutions were prepared using ultrapure water obtained using a Millipore Milli-Q water purification system (Billerica, MA) operating at an electrical resistance of ≥18.2 MΩ cm.

Preparation of CuNCs. CuNCs were prepared in a MOPS buffer (15 mM MOPS; 50 mM NaCl; pH 7.6), to which 1 μM ssDNA poly-T40 and 2 mM ascorbic acid were preliminarily added. After the mixture was thoroughly blended, 0.1 mM CuSO₄ was slowly added, and the resulting solution was incubated at room temperature to form T40-CuNCs. For comparison, T20-CuNCs, T60-CuNCs, and pristine CuNPs were similarly prepared using ssDNA, poly-T20, poly-T60, and without DNA, respectively.

Characterization. TEM images were captured using a JEOL-2100F (200 kV) microscope and copper grids (JEOL, Japan). Raman spectra were measured using an inVia Raman spectrometer (Renishaw, UK). A 50× long-working-distance objective lens [numerical aperture (NA) 0.5] was used to focus the laser beam on the sample and collect the Raman signals in the backscattering mode. The 785-nm-wavelength line from a 50 mW Ar-ion laser was used as the excitation source. Fluorescence measurements were carried out at room temperature on a FluoroMax-4-TCSPEC fluorescence spectrophotometer (Horiba, Jobin Yvon, France). FTIR spectra were measured on an IRTTracer-100 spectrometer (Shimadzu, Japan) using a KBr pellet. UV-vis absorption spectra were recorded on a UV-1800 UV-vis spectrophotometer (Shimadzu, Japan). XPS spectra were recorded using an ultrahigh-vacuum setup (SES 2002, Gammatdata-Scienta) equipped with a monochromatic Al Kα X-ray source (15 kV, 10 mA emission current). The binding energies were calibrated based on the C 1s feature at 284.8 eV. NMR spectroscopy was performed using a WNM-1-400 MHz NMR spectrometer.

Electrocatalytic NO₃RR Tests. Electrocatalytic NO₃RR tests were performed using a typical three-electrode system connected to a CHI760E electrochemical workstation (CH Instruments, Inc., China) in a typical H-type cell. The as-synthesized catalysts were dispersed in a mixed solvent comprising water and ethanol (1:1, v/v) to form a bulk suspension (0.5 mg mL⁻¹). The working electrodes were fabricated by dropping the catalyst suspension (200 μL) onto a piece of clean carbon paper (1 × 1 cm²), which was subsequently coated with 50 μL of a 0.2% Nafion solution and dried at 60 °C. Ag/AgCl (saturated KCl) and Pt mesh were used as the reference and counter electrodes, respectively. The electrolytes comprised Ar-saturated 1 M KOH containing different NO₃⁻ concentrations. The LSV curves were scanned at 10 mV s⁻¹. All potentials were calibrated to the RHE reference scale using the equation $E_{\text{RHE}} = E_{\text{Ag/AgCl}} + 0.204 \text{ V} + 0.0591\text{pH}$. The current density was normalized to the geometric electrode surface (~1 cm²). Potentiostatic measurements were performed for 1 h in 30 mL of a cathode electrolyte, and the electrolyte was then stored at 4 °C for no more than 2 days before analysis. To assess the performance change of the T40-CuNCs during long-term cycling, the electrolyte (30 mL of 1 M KOH and 0.1 M nitrate) was collected for product analysis after each hour of electrolysis, and fresh electrolyte was used for the next 1-h cycle. The double-layer capacitance (C_{dl}) was determined by scanning cyclic voltammetry (CV) in the range 10–50 mV s⁻¹ in a nonfaradaic potential window. The plot of the capacitive anode and cathode current differences $[(j_a - j_c)/2]$ at a set potential versus the CV scan rates exhibited a linear relationship, and the slope represented C_{dl} .⁷²

In Situ Raman Measurements. The in situ Raman spectra were collected using a confocal Raman microscope at controlled potentials. Briefly, an electrolytic cell was fabricated using polytetrafluoroethylene (Teflon) and a round piece of quartz glass as a cover to protect the objective lens (Figure S17). A catalyst-modified Au electrode, a Pt wire, and an Ag/AgCl electrode were used as the working, counter, and reference electrodes, respectively. The working electrode surface was positioned 100–200 μm from the glass window. The in situ Raman measurements were conducted using an inVia Raman spectrometer (Renishaw, U.K.) controlled by WiRE 4.0 software. A 50× objective lens was used to focus a 785-nm-wavelength, 50 mW laser vertically across the glass and on the electrode surface. The average acquisition time for each spectrum was 5 min. The Raman peak areas were calculated using the Gaussian-function-based nonlinear fitting method.

NH₄⁺ Quantification and FE Calculation. The produced NH₃ was quantified using the indophenol blue method.⁷³ Typically, a certain volume of the electrolyte is withdrawn from the reaction cell and diluted to 2 mL. Then, 2 mL of a 1 M NaOH solution containing trisodium citrate dihydrate (5 wt %), salicylic acid (5 wt %) (stored at 4 °C), and 1 mL of freshly prepared 0.05 M NaClO were added. The mixed solution was shaken for a few seconds. Finally, 0.2 mL of a sodium nitroferricyanide solution (1 wt %; stored at 4 °C) was added for the color reaction. The resulting solution was stored at room temperature for 1 h and then measured using a UV-vis spectrophotometer. The absorbance at 655 nm was used to determine the NH₃ concentration according to a calibration curve prepared using a standard NH₄Cl solution dissolved in different volumes of 1 M KOH.

The produced NH₃ was further quantified using the ¹H NMR method to confirm the accuracy of NH₃ quantification. Briefly, 125 μL of the standard solution was mixed with 125 μL of 15 mM maleic acid in deuterated dimethyl sulfoxide (DMSO-*d*₆; 99.9 atom % D), 50 μL of 4 M H₂SO₄ in DMSO-*d*₆, and 750 μL of DMSO-*d*₆.

The yield rate was calculated by eq 1:

$$\text{yield} = cV/tS \quad (1)$$

where c is the product concentration, V is the electrolyte volume in the cathode compartment, t is the electrolysis time, and S is the working electrode surface.

The FE was calculated based on eq 2:

$$FE = \frac{nV_{\text{NH}_3}c_{\text{NH}_3}F}{it} \quad (2)$$

where i is the total current, n represents the number of electron transfers (i.e., 8) toward the formation of 1 mol of NH_3 , V_{NH_3} is the catholyte volume (mL), c_{NH_3} represents the NH_3 concentration (M), F is the Faraday constant ($96,485 \text{ C mol}^{-1}$), and t is the electrolysis time.

The selectivity was calculated based on eq 3:

$$\text{selectivity} = \frac{c}{\Delta c_{\text{NO}_3^-}} \times 100\% \quad (3)$$

where c is the concentration of $\text{NH}_4^+/\text{NO}_2^-$ and $\Delta c_{\text{NO}_3^-}$ is the concentration difference of NO_3^- before and after reduction.

^{15}N Isotope-Labeling Experiment. The isotope-labeling experiment was carried out in a 1 M KOH solution containing 0.1 M $^{15}\text{NO}_3^-$ (99% ^{15}N atoms) by chronoamperometry measurements for 4 h at -0.6 V (vs RHE), and the produced $^{15}\text{NH}_4^+$ was qualitatively measured using ^1H NMR (Bruker Avance 500 MHz) spectroscopy. Briefly, 125 μL of the electrolytes was mixed with 125 μL of 15 mM maleic acid in $\text{DMSO-}d_6$ (99.9 atom % D), 50 μL of 4 M H_2SO_4 in $\text{DMSO-}d_6$, and 750 μL of $\text{DMSO-}d_6$.

Number of Electron Transfers and Calculations. To elucidate the number of electrons and kinetics associated with the NO_3RR , LSV curves were obtained using a RDE and a glassy carbon electrode (0.1964 cm^2) deposited with a T40-CuNCs catalyst as the working electrode. A Pt wire and Ag/AgCl (in saturated KCl) were used as the counter and reference electrodes, respectively. According to the K–L equation, the current inverse ($1/i$) is linearly related to the inverse square root of the rotation rate ($\omega^{-1/2}$), as shown in eq 4:⁷⁴

$$\frac{1}{i_m} = \frac{1}{i_k} + \frac{1}{0.2nFD^{2/3}\nu^{-1/6}C\omega^{1/2}} \quad (4)$$

where i_k is the kinetic current of the NO_3RR , n is the number of electrons exchanged in the NO_3RR , F is the Faraday constant (96485 C mol^{-1}), D is the nitrate diffusion coefficient ($1.40 \times 10^{-5} \text{ cm}^2 \text{ s}^{-1}$), ω is the rotation rate, ν is the kinematic viscosity ($1 \times 10^{-6} \text{ m}^2 \text{ s}^{-1}$), and C is the nitrate bulk concentration. The n value can be evaluated from the K–L curve slope at each electrode potential.

Apparent Activation Energy of the NO_3RR . To extract the apparent activation energy (E_a) for the NO_3RR , the catalyst electrochemical measurements were conducted in a 1 M KOH solution containing 100 mM KNO_3 at different temperatures. For heterogeneous electrocatalytic reactions, the current density (j) can be expressed as a function of E_a according to eq 5:⁷⁵

$$j = A_a \exp\left(-\frac{E_a}{RT}\right) \quad (5)$$

where A_a is the apparent preexponential factor, R is the ideal gas constant ($8.314 \text{ J K}^{-1} \text{ mol}^{-1}$), and T is the temperature (K). Therefore, E_a can be further calculated by fitting the slope of the Arrhenius plot according to eq 6:⁷⁶

$$\left. \frac{\partial(\log j)}{\partial(1/T)} \right|_{\eta} = -\frac{E_a}{2.303R} \quad (6)$$

while the intercept of the $\log j$ vs $1/T$ plot is the logarithm of A_a .

■ ASSOCIATED CONTENT

SI Supporting Information

The Supporting Information is available free of charge at <https://pubs.acs.org/doi/10.1021/acsami.3c00511>.

TEM images and cluster diameter analysis of the CuNCs, XRD, XPS, CD, UV–vis, and NMR spectra, electrochemical performances and corresponding analyses, pH variation, in situ Raman spectra and related

analyses, kinetic studies, and comparisons of the catalytic activities for the T40-CuNCs and other Cu-based catalysts (PDF)

■ AUTHOR INFORMATION

Corresponding Authors

Yongjie Ge – Key Laboratory of Carbon Materials of Zhejiang Province, Wenzhou University, Wenzhou 325035, China;

orcid.org/0000-0002-2959-2914;

Email: geyongjie1220@126.com

Huagui Nie – Key Laboratory of Carbon Materials of Zhejiang Province, Wenzhou University, Wenzhou 325035, China; Email: huaguinie@126.com

Zhi Yang – Key Laboratory of Carbon Materials of Zhejiang Province, Wenzhou University, Wenzhou 325035, China;

orcid.org/0000-0002-9265-5041; Email: yang201079@126.com

Authors

Wenjie Luo – Key Laboratory of Carbon Materials of Zhejiang Province, Wenzhou University, Wenzhou 325035, China

Shilu Wu – Key Laboratory of Carbon Materials of Zhejiang Province, Wenzhou University, Wenzhou 325035, China

Yingyang Jiang – Key Laboratory of Carbon Materials of Zhejiang Province, Wenzhou University, Wenzhou 325035, China

Peng Xu – Key Laboratory of Carbon Materials of Zhejiang Province, Wenzhou University, Wenzhou 325035, China

Jinxuan Zou – Key Laboratory of Carbon Materials of Zhejiang Province, Wenzhou University, Wenzhou 325035, China

Jinjie Qian – Key Laboratory of Carbon Materials of Zhejiang Province, Wenzhou University, Wenzhou 325035, China;

orcid.org/0000-0002-9996-7929

Xuemei Zhou – Key Laboratory of Carbon Materials of Zhejiang Province, Wenzhou University, Wenzhou 325035, China

Complete contact information is available at:

<https://pubs.acs.org/doi/10.1021/acsami.3c00511>

Author Contributions

Y.G., H.N., and Z.Y. conceived the idea for this work and guided the projects. W.L. prepared the ssDNA poly-T-CuNCs catalysts and conducted the electrochemical measurements. S.W. performed activation energy measurements. Y.J., P.X., and J.Z. completed the in situ FTIR and Raman measurements and helped to discuss the data. J.Q. and X.Z. provided helpful advice and critical discussions. All authors discussed the results and commented on the manuscript.

Notes

The authors declare no competing financial interest.

■ ACKNOWLEDGMENTS

This work was supported by the National Science Foundation of China (Nos. 22105147, 21875166, and U21A2081).

■ REFERENCES

- Valera-Medina, A.; Xiao, H.; Owen-Jones, M.; David, W. I. F.; Bowen, P. J. Ammonia for Power. *Prog. Energy Combust. Sci.* **2018**, *69*, 63–102.

- (2) Wang, M.; Khan, M. A.; Mohsin, I.; Wicks, J.; Ip, A. H.; Sumon, K. Z.; Dinh, C. T.; Sargent, E. H.; Gates, I. D.; Kibria, M. G. Can Sustainable Ammonia Synthesis Pathways Compete with Fossil-Fuel Based Haber-Bosch Processes? *Energy Environ. Sci.* **2021**, *14*, 2535–2548.
- (3) Chen, C.; Yan, D.; Wang, Y.; Zhou, Y.; Zou, Y.; Li, Y.; Wang, S. B-N Pairs Enriched Defective Carbon Nanosheets for Ammonia Synthesis with High Efficiency. *Small* **2019**, *15*, No. 1805029.
- (4) Erisman, J. W.; Sutton, M. A.; Galloway, J.; Klimont, Z.; Winiwarter, W. How a Century of Ammonia Synthesis Changed the World. *Nature Geosci.* **2008**, *1*, 636–639.
- (5) Hirakawa, H.; Hashimoto, M.; Shiraiishi, Y.; Hirai, T. Selective Nitrate-to-Ammonia Transformation on Surface Defects of Titanium Dioxide Photocatalysts. *ACS Catal.* **2017**, *7*, 3713–3720.
- (6) Garcia-Segura, S.; Lanzarini-Lopes, M.; Hristovski, K.; Westerhoff, P. Electrocatalytic Reduction of Nitrate: Fundamentals to Full-Scale Water Treatment Applications. *Appl. Catal., B* **2018**, *236*, 546–568.
- (7) Wang, Y.; Yu, Y.; Jia, R.; Zhang, C.; Zhang, B. Electrochemical Synthesis of Nitric Acid from Air and Ammonia through Waste Utilization. *Natl. Sci. Rev.* **2019**, *6*, 730–738.
- (8) Wang, Z.; Richards, D.; Singh, N. Recent Discoveries in the Reaction Mechanism of Heterogeneous Electrocatalytic Nitrate Reduction. *Catal. Sci. Technol.* **2021**, *11*, 705–725.
- (9) Wang, Y.; Wang, C.; Li, M.; Yu, Y.; Zhang, B. Nitrate Electroreduction: Mechanism Insight, In Situ Characterization, Performance Evaluation, and Challenges. *Chem. Soc. Rev.* **2021**, *50*, 6720–6733.
- (10) Zhang, X.; Wang, Y.; Liu, C.; Yu, Y.; Lu, S.; Zhang, B. Recent Advances in Non-Noble Metal Electrocatalysts for Nitrate Reduction. *Chem. Eng. J.* **2021**, *403*, 126269.
- (11) Khomutov, N. E.; Stamkulov, U. S. Nitrate Reduction at Various Metal Electrodes. *Sov. Electrochem.* **1971**, *7*, 312–316.
- (12) Zhang, X.; Wang, C.; Guo, Y.; Zhang, B.; Wang, Y.; Yu, Y. Cu Clusters/TiO_{2-x} with Abundant Oxygen Vacancies for Enhanced Electrocatalytic Nitrate Reduction to Ammonia. *J. Mater. Chem. A* **2022**, *10*, 6448–6453.
- (13) Yu, C. L.; Chen, H. Y.; Lo, N. C.; Lee, C. L.; Chen, P. Y. Enhanced Catalytic Activity of Copper Nanoparticles Electrochemically Co-Deposited with Cadmium towards the Electroreduction of Nitrate. *J. Electroanal. Chem.* **2022**, *914*, 116325.
- (14) de Groot, M. T.; Koper, M. T. M. The Influence of Nitrate Concentration and Acidity on the Electrocatalytic Reduction of Nitrate on Platinum. *J. Electroanal. Chem.* **2004**, *562*, 81–94.
- (15) Hu, T.; Wang, C.; Wang, M.; Li, C. M.; Guo, C. Theoretical Insights into Superior Nitrate Reduction to Ammonia Performance of Copper Catalysts. *ACS Catal.* **2021**, *11*, 14417–14427.
- (16) Xu, H.; Ma, Y.; Chen, J.; Zhang, W. X.; Yang, J. Electrocatalytic Reduction of Nitrate - A Step towards a Sustainable Nitrogen Cycle. *Chem. Soc. Rev.* **2022**, *51*, 2710–2758.
- (17) Katsounaros, I.; Kyriacou, G. Influence of Nitrate Concentration on Its Electrochemical Reduction on Tin Cathode: Identification of Reaction Intermediates. *Electrochim. Acta* **2008**, *53*, 5477–5484.
- (18) de Vooy, A. C. A.; Koper, M. T. M.; van Santen, R. A.; van Veen, J. A. R. Mechanistic Study of the Nitric Oxide Reduction on a Polycrystalline Platinum Electrode. *Electrochim. Acta* **2001**, *46*, 923–930.
- (19) Simpson, B. K.; Johnson, D. C. Electrocatalysis of Nitrate Reduction at Copper-Nickel Alloy Electrodes in Acidic Media. *Electroanalysis* **2004**, *16*, 532–538.
- (20) Xu, Y.; Ren, K.; Ren, T.; Wang, M.; Liu, M.; Wang, Z.; Li, X.; Wang, L.; Wang, H. Cooperativity of Cu and Pd Active Sites in CuPd Aerogels Enhances Nitrate Electroreduction to Ammonia. *Chem. Commun.* **2021**, *57*, 7525–7528.
- (21) Liu, H.; Lang, X.; Zhu, C.; Timoshenko, J.; Rüscher, M.; Bai, L.; Guijarro, N.; Yin, H.; Peng, Y.; Li, J.; Liu, Z.; Wang, W.; Cuenya, B. R.; Luo, J. Efficient Electrochemical Nitrate Reduction to Ammonia with Copper-Supported Rhodium Cluster and Single-Atom Catalysts. *Angew. Chem., Int. Ed.* **2022**, *61*, No. e202202556.
- (22) Chen, F. Y.; Wu, Z. Y.; Gupta, S.; Rivera, D. J.; Lamberts, S. V.; Pecaut, S.; Kim, J. Y. T.; Zhu, P.; Finfrock, Y. Z.; Meira, D. M.; King, G.; Gao, G.; Xu, W.; Cullen, D. A.; Zhou, H.; Han, Y.; Perea, D. E.; Muhich, C. L.; Wang, H. Efficient Conversion of Low-Concentration Nitrate Sources into Ammonia on a Ru-Dispersed Cu Nanowire Electrocatalyst. *Nat. Nanotechnol.* **2022**, *17*, 759–767.
- (23) Xu, Y. T.; Han, Y.; Sam, D. K.; Cao, Y. The Selective Electrocatalytic Reduction of Nitrate to Ammonia Using Co(ii)-Decorated TiO₂ Nanosheets. *J. Mater. Chem. A* **2022**, *10*, 22390–22398.
- (24) Wang, Y.; Zhou, W.; Jia, R.; Yu, Y.; Zhang, B. Unveiling the Activity Origin of a Copper-based Electrocatalyst for Selective Nitrate Reduction to Ammonia. *Angew. Chem., Int. Ed.* **2020**, *59*, 5350–5354.
- (25) Li, P.; Jiang, Y.; Hu, Y.; Men, Y.; Liu, Y.; Cai, W.; Chen, S. Hydrogen Bond Network Connectivity in the Electric Double Layer Dominates the Kinetic pH Effect in Hydrogen Electrocatalysis on Pt. *Nat. Catal.* **2022**, *5*, 900–911.
- (26) Strmcnik, D.; Uchimura, M.; Wang, C.; Subbaraman, R.; Danilovic, N.; van der Vliet, D.; Paulikas, A. P.; Stamenkovic, V. R.; Markovic, N. M. Improving the Hydrogen Oxidation Reaction Rate by Promotion of Hydroxyl Adsorption. *Nat. Chem.* **2013**, *5*, 300–306.
- (27) Danilovic, N.; Subbaraman, R.; Strmcnik, D.; Chang, K. C.; Paulikas, A. P.; Stamenkovic, V. R.; Markovic, N. M. Enhancing the Alkaline Hydrogen Evolution Reaction Activity through the Bifunctionality of Ni(OH)₂/Metal Catalysts. *Angew. Chem., Int. Ed.* **2012**, *51*, 12495–12498.
- (28) Subbaraman, R.; Tripkovic, D.; Chang, K. C.; Strmcnik, D.; Paulikas, A. P.; Hirunsit, P.; Chan, M.; Greeley, J.; Stamenkovic, V.; Markovic, N. M. Trends in Activity for the Water Electrolyser Reactions on 3d M(Ni,Co,Fe,Mn) Hydr(oxy)oxide Catalysts. *Nat. Mater.* **2012**, *11*, 550–557.
- (29) Berggren, G.; Adamska, A.; Lambert, C.; Simmons, T. R.; Esselborn, J.; Atta, M.; Gambarelli, S.; Mouesca, J. M.; Reijerse, E.; Lubitz, W.; Happe, T.; Artero, V.; Fontecave, M. Biomimetic Assembly and Activation of [FeFe]-Hydrogenases. *Nature* **2013**, *499*, 66–69.
- (30) Supekar, S.; Gamiz-Hernandez, A. P.; Kaila, V. R. I. A Protonated Water Cluster as a Transient Proton-Loading Site in Cytochrome c Oxidase. *Angew. Chem., Int. Ed.* **2016**, *55*, 11940–11944.
- (31) Wikstrom, M.; Krab, K.; Sharma, V. Oxygen Activation and Energy Conservation by Cytochrome c Oxidase. *Chem. Rev.* **2018**, *118*, 2469–2490.
- (32) Li, X.; Lv, B.; Zhang, X. P.; Jin, X.; Guo, K.; Zhou, D.; Bian, H.; Zhang, W.; Apfel, U. P.; Cao, R. Introducing Water-Network-Assisted Proton Transfer for Boosted Electrocatalytic Hydrogen Evolution with Cobalt Corrole. *Angew. Chem., Int. Ed.* **2022**, *61*, No. e202114310.
- (33) Umena, Y.; Kawakami, K.; Shen, J. R.; Kamiya, N. Crystal Structure of Oxygen-Evolving Photosystem II at a Resolution of 1.9 Å. *Nature* **2011**, *473*, 55–60.
- (34) Wikstrom, M.; Sharma, V.; Kaila, V. R.; Hosler, J. P.; Hummer, G. New Perspectives on Proton Pumping in Cellular Respiration. *Chem. Rev.* **2015**, *115*, 2196–2221.
- (35) Liu, G.; Shao, Y.; Peng, J.; Dai, W.; Liu, L.; Xu, S.; Wu, F.; Wu, X. Highly Thymine-Dependent Formation of Fluorescent Copper Nanoparticles Templated By ss-DNA. *Nanotechnology* **2013**, *24*, 345502.
- (36) Qing, Z.; He, X.; He, D.; Wang, K.; Xu, F.; Qing, T.; Yang, X. Poly(thymine)-Templated Selective Formation of Fluorescent Copper Nanoparticles. *Angew. Chem., Int. Ed.* **2013**, *52*, 9719–9722.
- (37) Xu, Y. T.; Xie, M. Y.; Zhong, H.; Cao, Y. In Situ Clustering of Single-Atom Copper Precatalysts in a Metal-Organic Framework for Efficient Electrocatalytic Nitrate-to-Ammonia Reduction. *ACS Catal.* **2022**, *12*, 8698–8706.
- (38) Karthik, K.; Anantharaj, S.; Karthik, P. E.; Subramanian, B.; Kundu, S. Self-Assembled Molecular Hybrids of CoS-DNA for

Enhanced Water Oxidation with Low Cobalt Content. *Inorg. Chem.* **2017**, *56*, 6734–6745.

(39) Jurca, T.; Marian, E.; Vicaș, L. G.; Mureșan, M. E.; Fritea, L. Metal Complexes of Pharmaceutical Substances. In *Spectroscopic Analyses—Developments and Applications*; Sharmin, E., Ed.; IntechOpen: Rijeka, Croatia, 2017; pp 123–124.

(40) Jurca, T.; Marian, E.; Cavalu, S. Raman and SERS Investigation of New Synthesized Nicotinic Acid Metallic Complexes. *Rev. Chim.* **2009**, *60*, 320–322.

(41) Jehlička, J.; Culka, A. Raman Spectra of Nitrogen-Containing Organic Compounds Obtained Using a Portable Instrument at -15°C at 2860 M Above Sea Level. *J. Raman Spectrosc.* **2010**, *41*, 537–542.

(42) Mao, Y.; He, J.; Sun, X.; Li, W.; Lu, X.; Gan, J.; Liu, Z.; Gong, L.; Chen, J.; Liu, P.; Tong, Y. Electrochemical Synthesis of Hierarchical Cu_2O Stars with Enhanced Photoelectrochemical Properties. *Electrochim. Acta* **2012**, *62*, 1–7.

(43) Hsu, Y. K.; Yu, C. H.; Chen, Y. C.; Lin, Y. G. Fabrication of Coral-Like Cu_2O Nanoelectrode for Solar Hydrogen Generation. *J. Power Sources* **2013**, *242*, 541–547.

(44) Majumdar, D.; Singha, A.; Mondal, P. K.; Kundu, S. DNA-Mediated Wirelike Clusters of Silver Nanoparticles: An Ultrasensitive SERS Substrate. *ACS Appl. Mater. Interfaces* **2013**, *5*, 7798–7807.

(45) Su, Y. T.; Lan, G. Y.; Chen, W. Y.; Chang, H. T. Detection of Copper Ions Through Recovery of the Fluorescence of DNA-Templated Copper/Silver Nanoclusters in the Presence of Mercapto-propionic Acid. *Anal. Chem.* **2010**, *82*, 8566–8572.

(46) Wu, Z. Y.; Karamad, M.; Yong, X.; Huang, Q.; Cullen, D. A.; Zhu, P.; Xia, C.; Xiao, Q.; Shakouri, M.; Chen, F. Y.; Kim, J. Y. T.; Xia, Y.; Heck, K.; Hu, Y.; Wong, M. S.; Li, Q.; Gates, I.; Siahrostami, S.; Wang, H. Electrochemical Ammonia Synthesis via Nitrate Reduction on Fe Single Atom Catalyst. *Nat. Commun.* **2021**, *12*, 2870.

(47) Pletcher, D.; Poorabedi, Z. The Reduction of Nitrate at a Copper Cathode in Aqueous Acid. *Electrochim. Acta* **1979**, *24*, 1253–1256.

(48) Reyter, D.; Chamoulaud, G.; Bélanger, D.; Roué, L. Electrochemical Reduction of Nitrate on Copper Electrodes Prepared by High-Energy Ball Milling. *J. Electroanal. Chem.* **2006**, *596*, 13–24.

(49) Mattarozzi, L.; Cattarin, S.; Comisso, N.; Gambirasi, A.; Guerriero, P.; Musiani, M.; Vázquez-Gómez, L.; Verlató, E. Hydrogen Evolution Assisted Electrodeposition of Porous Cu-Ni Alloy Electrodes and Their Use for Nitrate Reduction in Alkali. *Electrochim. Acta* **2014**, *140*, 337–344.

(50) Chen, G. F.; Yuan, Y.; Jiang, H.; Ren, S. Y.; Ding, L. X.; Ma, L.; Wu, T.; Lu, J.; Wang, H. Electrochemical Reduction of Nitrate to Ammonia via Direct Eight-Electron Transfer Using a Copper-Molecular Solid Catalyst. *Nat. Energy* **2020**, *5*, 605–613.

(51) Fu, X.; Zhao, X.; Hu, X.; He, K.; Yu, Y.; Li, T.; Tu, Q.; Qian, X.; Yue, Q.; Wasielewski, M. R.; Kang, Y. Alternative Route for Electrochemical Ammonia Synthesis by Reduction of Nitrate on Copper Nanosheets. *Appl. Mater. Today* **2020**, *19*, 100620.

(52) Hu, Q.; Qin, Y.; Wang, X.; Wang, Z.; Huang, X.; Zheng, H.; Gao, K.; Yang, H.; Zhang, P.; Shao, M.; He, C. Reaction Intermediate-Mediated Electrocatalyst Synthesis Favors Specified Facet and Defect Exposure for Efficient Nitrate-Ammonia Conversion. *Energy Environ. Sci.* **2021**, *14*, 4989–4997.

(53) Li, L. X.; Sun, W. J.; Zhang, H. Y.; Wei, J. L.; Wang, S. X.; He, J. H.; Li, N. J.; Xu, Q. F.; Chen, D. Y.; Li, H.; Lu, J. M. Highly Efficient and Selective Nitrate Electroreduction to Ammonia Catalyzed by Molecular Copper Catalyst@ $\text{Ti}_3\text{C}_2\text{Tx}$ MXene. *J. Mater. Chem. A* **2021**, *9*, 21771–21778.

(54) Ren, T.; Ren, K.; Wang, M.; Liu, M.; Wang, Z.; Wang, H.; Li, X.; Wang, L.; Xu, Y. Concave-Convex Surface Oxide Layers Over Copper Nanowires Boost Electrochemical Nitrate-to-Ammonia Conversion. *Chem. Eng. J.* **2021**, *426*, 130759.

(55) Wang, C.; Liu, Z.; Hu, T.; Li, J.; Dong, L.; Du, F.; Li, C.; Guo, C. Metasequoia-Like Nanocrystal of Iron-Doped Copper for Efficient Electrocatalytic Nitrate Reduction into Ammonia in Neutral Media. *ChemSusChem* **2021**, *14*, 1825–1829.

(56) Fu, W.; Hu, Z.; Zheng, Y.; Su, P.; Zhang, Q.; Jiao, Y.; Zhou, M. Tuning Mobility of Intermediate and Electron Transfer to Enhance Electrochemical Reduction of Nitrate to Ammonia on $\text{Cu}_2\text{O}/\text{Cu}$ Interface. *Chem. Eng. J.* **2022**, *433*, 133680.

(57) Wang, C.; Ye, F.; Shen, J.; Xue, K. H.; Zhu, Y.; Li, C. In Situ Loading of Cu_2O Active Sites on Island-Like Copper for Efficient Electrochemical Reduction of Nitrate to Ammonia. *ACS Appl. Mater. Interfaces* **2022**, *14*, 6680–6688.

(58) Bae, S. E.; Stewart, K. L.; Gewirth, A. A. Nitrate Adsorption and Reduction on $\text{Cu}(100)$ in Acidic Solution. *J. Am. Chem. Soc.* **2007**, *129*, 10171–10180.

(59) Butcher, D. P.; Gewirth, A. A. Nitrate Reduction Pathways on Cu Single Crystal Surfaces: Effect of Oxide and Cl^- . *Nano Energy* **2016**, *29*, 457–465.

(60) Molodkina, E. B.; Ehrenburg, M. R.; Polukarov, Y. M.; Danilov, A. I.; Souza-Garcia, J.; Feliu, J. M. Electroreduction of Nitrate Ions on Pt(111) Electrodes Modified by Copper Adatoms. *Electrochim. Acta* **2010**, *56*, 154–165.

(61) Bhattacharjee, S.; Waghmare, U. V.; Lee, S. C. An Improved D-Band Model of the Catalytic Activity of Magnetic Transition Metal Surfaces. *Sci. Rep.* **2016**, *6*, 35916.

(62) Li, X.; Shen, P.; Li, X.; Ma, D.; Chu, K. Sub-nm RuO_x Clusters on Pd Metallene for Synergistically Enhanced Nitrate Electroreduction to Ammonia. *ACS Nano* **2023**, *17*, 1081–1090.

(63) Fan, K.; Xie, W.; Li, J.; Sun, Y.; Xu, P.; Tang, Y.; Li, Z.; Shao, M. Active Hydrogen Boosts Electrochemical Nitrate Reduction to Ammonia. *Nat. Commun.* **2022**, *13*, 7958.

(64) Andersen, S. Z.; Čolić, V.; Yang, S.; Schwalbe, J. A.; Nielander, A. C.; McEnaney, J. M.; Enemark-Rasmussen, K.; Baker, J. G.; Singh, A. R.; Rohr, B. A.; Statt, M. J.; Blair, S. J.; Mezzavilla, S.; Kibsgaard, J.; Vesborg, P. C. K.; Cargnello, M.; Bent, S. F.; Jaramillo, T. F.; Stephens, I. E. L.; Nørskov, J. K.; Chorkendorff, I. A Rigorous Electrochemical Ammonia Synthesis Protocol with Quantitative Isotope Measurements. *Nature* **2019**, *570*, 504–508.

(65) Osmieri, L.; Monteverde Videla, A. H. A.; Ocón, P.; Specchia, S. Kinetics of Oxygen Electroreduction on Me-N-C (Me = Fe, Co, Cu) Catalysts in Acidic Medium: Insights on the Effect of the Transition Metal. *J. Phys. Chem. C* **2017**, *121*, 17796–17817.

(66) Wang, M.; Dong, C. L.; Huang, Y. C.; Li, Y.; Shen, S. Electronic Structure Evolution in Tricomponent Metal Phosphides with Reduced Activation Energy for Efficient Electrocatalytic Oxygen Evolution. *Small* **2018**, *14*, No. 1801756.

(67) Anantharaj, S.; Sugime, H.; Chen, B.; Akagi, N.; Noda, S. Achieving Increased Electrochemical Accessibility and Lowered Oxygen Evolution Reaction Activation Energy for Co^{2+} Sites with a Simple Anion Preoxidation. *J. Phys. Chem. C* **2020**, *124*, 9673–9684.

(68) Huang, J.; Sheng, H.; Ross, R. D.; Han, J.; Wang, X.; Song, B.; Jin, S. Modifying Redox Properties and Local Bonding of Co_3O_4 by CeO_2 Enhances Oxygen Evolution Catalysis in Acid. *Nat. Commun.* **2021**, *12*, 3036.

(69) Julien, C. Raman Spectra of Birnessite Manganese Dioxides. *Solid State Ionics* **2003**, *159*, 345–356.

(70) Kneipp, J.; Kneipp, H.; McLaughlin, M.; Brown, D.; Kneipp, K. In Vivo Molecular Probing of Cellular Compartments with Gold Nanoparticles and Nanoaggregates. *Nano Lett.* **2006**, *6*, 2225–2231.

(71) Xu, Y. T.; Peng, Z.; Han, Y.; Zhong, H.; Yang, J.; Cao, Y. Insight into Hydrogenation Selectivity of the Electrocatalytic Nitrate-to-Ammonia Reduction Reaction via Enhancing the Proton Transport. *ChemSusChem* **2022**, *15*, No. e202102450.

(72) Hu, Q.; Wang, Z.; Huang, X.; Qin, Y.; Yang, H.; Ren, X.; Zhang, Q.; Liu, J.; He, C. A Unique Space Confined Strategy to Construct Defective Metal Oxides within Porous Nanofibers for Electrocatalysis. *Energy Environ. Sci.* **2020**, *13*, 5097–5103.

(73) Wang, J.; Yu, L.; Hu, L.; Chen, G.; Xin, H.; Feng, X. Ambient Ammonia Synthesis via Palladium-Catalyzed Electrohydrogenation of Dinitrogen at Low Overpotential. *Nat. Commun.* **2018**, *9*, 1795.

(74) Wang, Y.; Xu, A.; Wang, Z.; Huang, L.; Li, J.; Li, F.; Wicks, J.; Luo, M.; Nam, D. H.; Tan, C. S.; Ding, Y.; Wu, J.; Lum, Y.; Dinh, C. T.; Sinton, D.; Zheng, G.; Sargent, E. H. Enhanced Nitrate-to-

Ammonia Activity on Copper-Nickel Alloys via Tuning of Intermediate Adsorption. *J. Am. Chem. Soc.* **2020**, *142*, 5702–5708.

(75) Anderson, A. B.; Roques, J.; Mukerjee, S.; Murthi, V. S.; Markovic, N. M.; Stamenkovic, V. Activation Energies for Oxygen Reduction on Platinum Alloys: Theory and Experiment. *J. Phys. Chem. B* **2005**, *109*, 1198–1203.

(76) Suermann, M.; Schmidt, T. J.; Büchi, F. N. Comparing the Kinetic Activation Energy of the Oxygen Evolution and Reduction Reactions. *Electrochim. Acta* **2018**, *281*, 466–471.